Effects of spanwise rotation on the structure of two-dimensional fully developed turbulent channel flow

By JAMES P. JOHNSTON, ROBERT M. HALLEEN†
AND DIETRICH K. LEZIUS‡

Department of Mechanical Engineering, Stanford University

Experiments on fully developed turbulent flow in a channel which is rotating at a steady rate about a spanwise axis are described. The Coriolis force components in the region of two-dimensional mean flow affect both local and global stability. Three stability-related phenomena were observed or inferred: (i) the reduction (increase) of the rate of wall-layer streak bursting in locally stabilized (destabilized) wall layers; (ii) the total suppression of transition to turbulence in a stabilized layer; (iii) the development of large-scale roll cells on the destabilized side of the channel by growth of a Taylor–Gortler vortex instability.

An appropriate local stability parameter is the Richardson number formulated by Bradshaw (1969) for this case and the analogous cases of flow over curved walls and of shear-layer flow with density stratification. Local effects of rotational stabilization, such as reduction of the turbulent stress in wall layers, can be related to the local Richardson number in a simple way. This paper not only investigates this effect, but also, by methods of flow visualization, exposes some of the underlying structure changes caused by rotation.

1. Introduction

The study of flows, viscous and inviscid, in blade passages of radial flow pump and compressor impellers has interested many engineers who wished to improve the efficiency of these devices. Impeller flow is most easily analysed in a reference frame that rotates with the blades so that the mean flow field may be assumed steady. However, co-ordinate rotation requires the inclusion of centrifugal and Coriolis accelerations in the equations of motion. If only laminar motion need be considered, the inclusion of these accelerations (forces) would cause little concern. However, as we hope to demonstrate, basic and complex changes of flow regime and structure in the turbulent boundary layer may result from system rotation.

It was pointed out in a recent review, Johnston (1970), that there are two basic effects associated with boundary layers on rotating surfaces. (i) If components of the Coriolis acceleration exist parallel to the solid surfaces on which the layers

---

† Present address: Caterpillar Tractor Co., Peoria, Illinois.
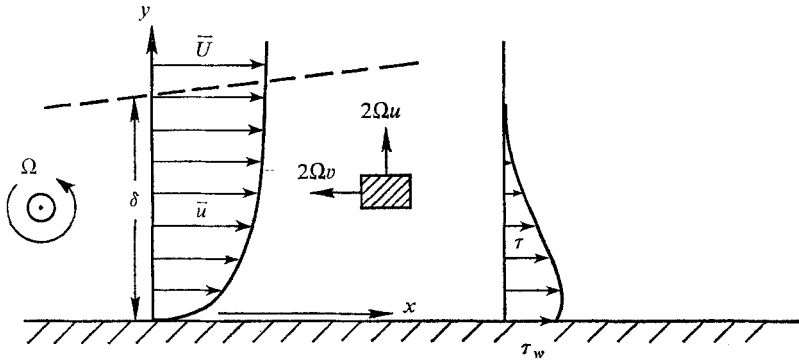‡ Present address: NASA/Ames Research Center, California.

FIGURE 1. Mean velocity and total shear-stress profiles for a two-dimensional boundary layer on a rotating surface. Layer unstable with $\Omega > 0$, as shown. Vectors on particle are Coriolis accelerations.

are growing, three-dimensionality, i.e. secondary flows, will tend to develop in the mean flow field of the layers. (ii) If a component of the Coriolis acceleration is perpendicular to a solid surface, less well understood stabilizing effects are observed in the turbulence structure itself. Both effects are believed to be important in the flow fields of centrifugal impellers (see Dean 1968).

The phenomena associated with the stabilization effect are to be discussed here. In the simplest sense, stabilization arises from the spring-like nature of the net effects of Coriolis forces. Consider the case of a typical boundary layer on a rotating wall (see figure 1). If the rotation and fluid velocity vectors have a given orientation, fluid particles perturbed along a normal to the wall tend to be 'forced' back to their equilibrium positions as though connected by 'springs' of positive constant. However, reversal of the rotation rate vector with respect to the fluid velocity vector can destabilize the flow by making the 'springs' have negative constants. Exact stability analysis of straight rotating shear flows is considered in Lezius (1971), where these ideas and other more precise analogies are discussed.

We have observed three different stability-related phenomena in bound rotating shear flows. (i) Rotation can, by a change in the wall-layer streak burst rate, modify the rate of turbulence production relative to dissipation and thereby modify the profiles of turbulence energy, stress and mean velocity across the layer in a manner closely analogous to that observed in curved shear layers (see Bradshaw 1969). (ii) Rotation can decrease the tendency of a hydrodynamically unstable laminar layer to undergo transition to a turbulent state, i.e. rotation can suppress turbulent transition (see Johnston 1971). (iii) Finally, as shown by Potter & Chawla (1971) for laminar boundary layers and by Hart (1971) for laminar channel flows, rotation may induce instability of the flow to large-scale disturbances. We have seen the development of large cellular vortical modes of the Taylor–Gortler type, which are called roll cells in this paper.

Here we shall deal explicitly with experimental observations on these three phenomena that have been described in detail by Halleen (1967) and by Lezius (1971). The experiments were conducted with water flowing at low speed in a

simple straight parallel-walled channel apparatus mounted so that it could be rotated at a steady rate about an axis normal to the plane of mean shear. The channel was long enough so that the mean flow was nearly fully developed. The channel depth between end walls was large enough so that the flow in its central third was nearly two-dimensional in the time mean, e.g. the central flow region was essentially uneffected by end-wall and corner secondary flows.

Water was chosen as a working fluid so that detailed flow studies could be carried out using both the dye and the hydrogen-bubble visualization methods. The results of the flow visualization studies are the principal output of the experiments. However, quantitative measurements of wall shear stress and mean velocity profiles were obtained by Halleen for various states of flow and rotation. Results deduced from the latter data will also be described to support those obtained by flow visualization.

The analytic studies of Johnston (1971) on the transition problem and the Taylor–Gortler stability analysis of Lezius (1971) will not be recounted here, but the brief consideration of the basic equations and parameters given in § 2 should help the reader to understand the results. A discussion of experimental apparatus and technique is given in § 3 and the appendix to provide background for the discussion of results in § 4. An attempt to summarize briefly our state of knowlege is given in the concluding section, § 5.

2. Theoretical background

Some understanding of the problem may be obtained by examination of the equations of motion for a two-dimensional turbulent boundary layer of thickness δ (see figure 1). The layer is assumed to grow on a flat surface which rotates at steady angular velocity Ω about an axis that is perpendicular to the plane of mean shear, i.e. the plane containing the mean shear stress. This stress is the sum of the laminar stress and the Reynolds stress:

$$\tau = \mu \, \partial \overline{u}/\partial y - \rho \overline{u'v'}. \tag{1}$$

The fluid velocity components relative to co-ordinates (x, y, z) that rotate with the surface are the sums of mean and fluctuating parts: $u = \overline{u} + u'$, $v = \overline{v} + v'$ and $w = w'$. Two-dimensional mean flow where $\overline{w} = 0$ and where the z axis is parallel to the axis of rotation is assumed. The static pressure in the fluid is similarly represented: $p = \overline{p} + p'$. Finally, an incompressible fluid of density ρ and constant kinematic viscosity ν will be assumed.

A convenient simplification ensues for an incompressible fluid in rotating co-ordinates when the reduced mean static pressure $\overline{p}^*$ is used in the equations of motion. The definition of $\overline{p}^*$ is

$$\overline{p}^* = \overline{p} - \tfrac{1}{2}\rho \Omega^2 r^2,$$

and therefore
$$p^* = \overline{p}^* + p'.$$

The term $(\tfrac{1}{2}\rho\Omega^2 r^2)$ is the centrifugal force potential caused by system rotation. r is the distance of any point in the field from the axis of rotation. The value of r

and the centrifugal force are in fact irrelevant to consideration of the dynamics of motion for an incompressible fluid because the centrifugal force is in this case conservative. The only new force introduced is the Coriolis force – or acceleration, as we write the equations (see figure 1 and equations (2) below).

To the boundary-layer approximation, the mean-flow dynamic equations of motion in the x and y directions are

$$\frac{D\bar{u}}{Dt} - 2\Omega\bar{v} = -\frac{1}{\rho}\frac{\partial\overline{p^*}}{\partial x} + \frac{1}{\rho}\frac{\partial\tau}{\partial y}, \tag{2a}$$

$$+ 2\Omega\bar{u} = -\frac{1}{\rho}\frac{\partial\overline{p^*}}{\partial y} - \frac{\partial\overline{v'^2}}{\partial y}, \tag{2b}$$

where the convective derivative following the time-mean particle motion is

$$\frac{D}{Dt} = \frac{\partial}{\partial t} + \bar{u}\frac{\partial}{\partial x} + \bar{v}\frac{\partial}{\partial y}.$$

The time-mean continuity equation is

$$\frac{\partial\bar{u}}{\partial x} + \frac{\partial\bar{v}}{\partial y} = 0. \tag{3}$$

If the equations are normalized so that $D\bar{u}/Dt \simeq 1$ and are made dimensionless, the Coriolis acceleration $-2\Omega\bar{v}$ is of the order of a characteristic rotation number,† $Ro \triangleq 2|\Omega|\,\delta/U$. U is the value of the velocity $\bar{u}$ at the boundary-layer edge, where $y = \delta$. We shall use a closely related rotation number to characterize the magnitude of Coriolis effects in the experiments, where values of $Ro \leqslant 0.2$ covered the range of interest.

For very weak rotation, $Ro \leqslant 0.01$, it is a good approximation to drop the term $-2\Omega\bar{v}$ from (2a) and neglect $\partial\overline{p^*}/\partial y$ since, for these conditions,

$$|2\Omega\bar{u}| \leqslant |\partial\overline{v'^2}/\partial y|$$

in (2b), and the latter term is itself usually neglected in non-rotating flows; $\overline{v'^2} \leqslant 0.01\,U^2$ in most boundary layers.

In the range of relatively rapid rotations, $0.1 < Ro < 1$, the term $\partial\overline{v'^2}/\partial y$ may be dropped from (2b) since it should be an order of magnitude less than $2\Omega\bar{u}$. Equation (2b) may be integrated and the result inserted into (2a), so that

$$\frac{D\bar{u}}{Dt} - 2\Omega\bar{v} = -\frac{1}{\rho}\frac{d\overline{p_\delta^*}}{dx} + 2\Omega\int_y^\delta \bar{u}\,dy + \frac{1}{\rho}\frac{\partial\tau}{\partial y}. \tag{4}$$

$\overline{p_\delta^*}$ is the reduced pressure at the edge of the boundary layer. Given the free-stream pressure gradient, initial conditions and information on τ, equations (4) and (3), the continuity equation, are sufficient to solve for the mean-velocity field.

The solution of these equations would be relatively straightforward if we knew how $\overline{v'^2}$ and $-\rho\overline{u'v'}$, the Reynolds stress, varied across the layer. For non-rotating flows there are currently a number of reasonably simple approaches to

† *Ro*, the inverse of a Rossby number, represents the ratio of Coriolis forces to inertia forces.

computation ranging from the non-equilibrium method of Bradshaw, Ferris & Atwell (1967) to a variety of simple mixing-length methods. Questions we have attempted to study in our experiments are: how does change of rotation, Ro, at fixed Reynolds number affect basic flow structure and the structure-related quantitative variables, $-\overline{u'v'}$, the mixing length $l \triangleq (-\overline{u'v'})^{\frac{1}{2}}/(\partial\overline{u}/\partial y)$, eddy viscosity $\epsilon \triangleq -\overline{u'v'}/(\partial\overline{u}/\partial y)$, turbulence energy production rate $\hat{P}$, etc. necessary to understand, and ultimately solve, rotating-boundary-layer problems?

It is useful to start consideration of these matters by looking at the equations for the rates of increase of the turbulence correlations $\overline{u'^2}$, $\overline{v'^2}$, $\overline{w'^2}$ and $-\overline{u'v'}$ as we follow time-mean particle motion. These equations are developed in Townsend (1956) and other sources for the zero-rotation case. They are given in Halleen (1967) for general three-dimensional rotating flow and in detail in Johnston (1970) for fully developed two-dimensional channel flow. For the boundary-layer case they are

$$D(-\overline{u'v'})/Dt = +(\overline{v'^2})\,\partial\overline{u}/\partial y + (\overline{u'^2}-\overline{v'^2})\,2\Omega + [\text{O.T.}], \qquad (5a)$$

$$D(\overline{u'^2})/Dt = +(-\overline{u'v'})\,2\,\partial\overline{u}/\partial y - (-\overline{u'v'})\,4\Omega + [\text{O.T.}], \qquad (5b)$$

$$D(\overline{v'^2})/Dt = 0 + (-\overline{u'v'})\,4\Omega + [\text{O.T.}], \qquad (5c)$$

$$D(\overline{w'^2})/Dt = 0 + 0 + [\text{O.T}]. \qquad (5d)$$

The terms on the left-hand sides are the 'advection' or 'mean transport' terms. Just to the right of the equals sign are the well-known zero-rotation rate of 'production' terms. Next on the right are the rotation 'production' terms that enter (5) for rotating flow as a result of the Coriolis accelerations. Finally, all other terms are lumped together and designated [O.T.]. These terms include rates of viscous transport and dissipation, diffusion and convection by turbulence and the fluctuating pressure–strain interaction terms. All the [O.T.] terms are identical to their respective zero-rotation forms, see Townsend (1956).

The equation for development of turbulence energy,

$$\tfrac{1}{2}\overline{q^2} = \tfrac{1}{2}(\overline{u'^2}+\overline{v'^2}+\overline{w'^2}),$$

is obtained by taking one half of the sum of (5b), (5c) and (5d):

$$\frac{D(\tfrac{1}{2}\overline{q^2})}{Dt} = +(-\overline{u'v'})\frac{\partial\overline{u}}{\partial y} + [\text{O.T.}] = \hat{P} + [\text{O.T.}]. \qquad (6)$$

Production of turbulence energy $\hat{P}$ is not explicitly dependent upon Ω, but it is implicitly affected by rotation through the effects Ω has on Reynolds stress and mean shear.†

For boundary layers and channel flows, peak levels of turbulence energy and stress are achieved in the regions close to the solid walls, i.e. the wall layers. In the wall layers the production and dissipation terms in (5) and (6) are very large. The excess energy or stress produced locally is diffused, or transported, by the

† This result is obvious once one realizes that rotation provides no direct mechanism for energy transformation because Coriolis forces are always instantaneously perpendicular to the instantaneous fluid velocity vector.

non-dissipative parts of the [O.T.] terms. The advection terms are usually very small and may be neglected in the wall layers. Therefore the production terms are the only terms that can cause a local gain in the level of energy or stress. It is reasonable to assume, as a first approximation, that effects which increase (decrease) the appropriate net production rates will also lead to an increase (decrease) in levels of turbulence energy and stress.

Let us apply this idea to the rotating-boundary-layer case, see figure 1, where $\partial \bar{u}/\partial y$ is positive and the usual conditions exist, i.e. $-\overline{u'v'} > 0$ and $\overline{u'^2} - \overline{v'^2} > 0$. Also assume, for the moment, that the rotation rate is positive, $\Omega > 0$. It is seen from the rotation production terms in (5a) that positive rotation causes an increase in the net rate of production of turbulence stress. Consequently we expect that a layer with positive rotation will have a higher level of stress $-\overline{u'v'}$ than an otherwise equivalent stationary layer. If $-\overline{u'v'}$ is increased with positive rotation then the production of turbulence energy $\hat{P}$ will be higher and consequently the level of energy $\frac{1}{2}\overline{q^2}$ will increase. The direction of rotation is arbitrary. If it is negative, $\Omega < 0$, the same train of argument will indicate that rates of production of $-\overline{u'v'}$ and $\frac{1}{2}\overline{q^2}$ will tend to decrease relative to conditions that would exist in equivalent stationary flow.

In summary, further examination of the production terms in (5) and (6) leads us to conclude that in wall layers the sign, and the magnitude, of rotation effects might be controlled by a local dimensionless parameter

$$S \triangleq -\frac{2\Omega}{(\partial \bar{u}/\partial y)}, \tag{7}$$

so that when $S > 0$, decrease of $-\overline{u'v'}$ and $\frac{1}{2}\overline{q^2}$ is expected, but when $S < 0$, increase of $-\overline{u'v'}$ and $\frac{1}{2}\overline{q^2}$ is expected.

Finally, the question is, how is this parameter related to flow stability? Bradshaw (1969) provides an answer by examination of other turbulent shear flows with analogous non-conservative body forces: curved-streamline flows with centrifugal forces and density stratified flows with buoyant forces normal to the plane of flow. His conclusions are substantiated by Lezius (1971), who shows by direct examination of the linearized equations of hydrodynamic stability that local stability[†] may be enhanced when the gradient Richardson number[‡]

$$Ri \triangleq \frac{-2\Omega(\partial \bar{u}/\partial y - 2\Omega)}{(\partial \bar{u}/\partial y)^2} = S(S+1)$$

is positive. On the other hand, instability is enhanced when Ri is negative. In turbulent wall layers $\partial \bar{u}/\partial y$ is very large and for many practical flows $Ri \simeq S$ near the wall. Even though this simplification may not be true near the outer edge of a boundary layer, the approximation noted above is most accurate in the region of greatest interest, the wall layers, where turbulence energy production and dissipation are the greatest. In any case, positive S is always associated with

---

[†] Roughly defined as the tendency of disturbance magnitude to be limited (not dissipated) by the 'springiness' of the Coriolis forces.

[‡] Terminology used by Bradshaw (1969) in his discussion of the analogue to buoyant stability. We shall simply refer to this quantity as the Richardson number.
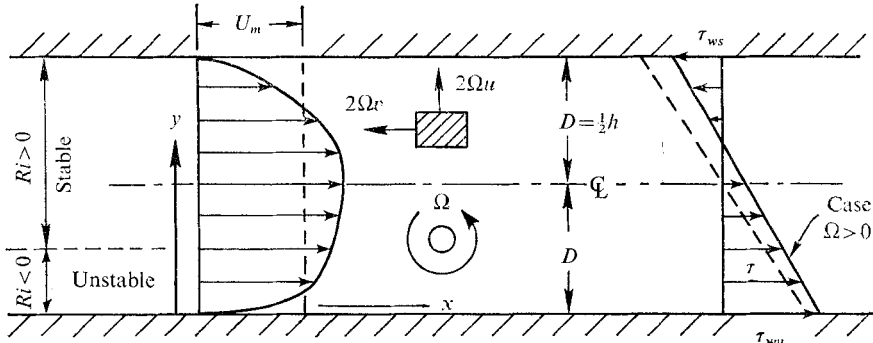
FIGURE 2. Mean velocity and total shear-stress profiles in fully developed two-dimensional rotating-channel flow.

stabilized flow, $Ri > 1$, and negative S with destabilized flow, $Ri < 1$, as long as S is greater than -1, which was the case in these investigations.

In the experiments we tried to establish time-mean steady fully developed two-dimensional channel flow (see figure 2). To this approximation, $D/Dt = 0$, $\bar{v} = 0$ and all x derivatives of mean velocities and velocity correlations may be dropped from the equations. Hence the left-hand sides of $(2a)$, (4), (5) and (6) all are zero. Equation $(2b)$ remains intact. Although the term $-2\Omega\bar{u}$ induces a pressure gradient normal to the channel walls, $\partial\overline{p^*}/\partial y$ is independent of x, and thus the term $\partial\overline{p^*}/\partial x$ in $(2a)$ is a negative constant. As a result, $(2a)$ may be integrated to give

$$\tau = \tau_{wu} + (\partial\overline{p^*}/\partial x)\,y, \tag{8a}$$

where, since $2D$ is the channel width,

$$\partial\overline{p^*}/\partial x = (\tau_{ws} - \tau_{wu})/2D. \tag{8b}$$

The signs of τ_{ws} and τ_{wu}, the wall shear stresses on the stable and unstable sides of the channel, depend upon the sign of Ω; τ_{wu} is positive and τ_{ws} negative for positive Ω as shown in figure 2. Reversal of Ω to clockwise ($\Omega < 0$) reverses the stable and unstable sides of the channel and the position and signs of τ_{ws} and τ_{wu}, e.g. subscripts u and s should be interchanged in $(8a)$ and $(8b)$.

The prime advantage of the fully developed channel-flow experiment is seen in $(8a)$; the shear stress profile is linear and can be obtained from measurement of the wall shear stresses. Thus, with measurement of mean velocity profiles, one can determine ϵ, l and $\hat{P}$ without the necessity of hot-wire anemometry or other complex instrumentation. A minor advantage is that flow visualization equipment (bubble wires, lights, mirrors, etc.) may be mounted on one wall of the channel and studies of both stabilization and destabilization phenomena made by simple change of rotation direction.

3. Experimental apparatus and techniques

Our channel flow apparatus is illustrated in three orthogonal views (figure 3). The channel itself is 1·54 in. wide in the principal shear plane, 59 in. long from the very abrupt contraction that joins it to the inlet plenum and 11 in. deep between
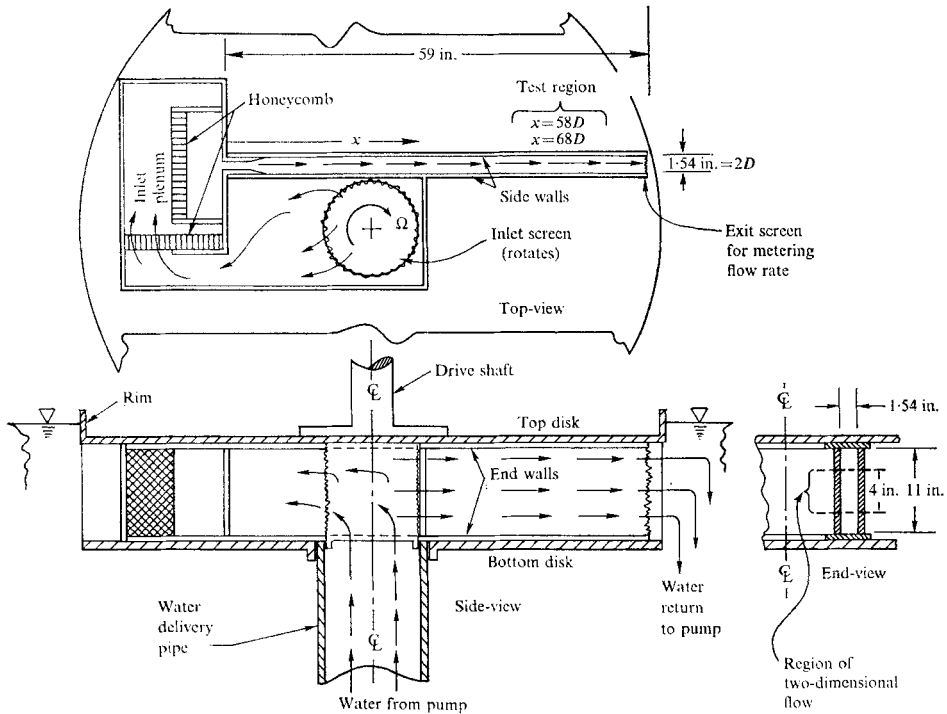
FIGURE 3. Rotating-channel-flow apparatus.

the end walls that are perpendicular to the axis of rotation. The transparent Plexiglas channel and plenum are fastened between two Plexiglas disks that can be driven in either direction about a central axis at any speed from $\frac{1}{4}$ to 20 r.p.m. This whole assembly is mounted in a large open tank with a Plexiglas bottom under which are banks of fluorescent lights used for dye visualization studies. A rim around the top disk keeps the upper surface dry so that instruments, cameras, etc. can be mounted above the channel. Both power and instrumentation slip rings are mounted on the drive shaft for remote control, and read-out purposes.

Filtered water is pumped from the laboratory sump into the axial delivery pipe. The water volume flow rate Q was measured by the indicated pressure drop across a perforated-plate screen at channel exit. The Q, ΔP characteristic of the screen was measured, in place, by direct flow weighing. Water returns from the tank to the laboratory sump by overflow ducts designed to hold the water slightly above the level of the upper surface of the top disk. Therefore, all the space below water level is filled both inside and outside of the channel.

In the test region of the channel, fully developed flow was indicated in the mean velocity profiles measured by Halleen at $x = 58D$ and $x = 68D$. Velocity profiles were almost all measured at the channel centre-plane, $5\frac{1}{2}$ in. from the end walls. However, check measurements at other spanwise stations, and wall-layer dye studies showed that secondary motions in the end-wall regions (Moore 1967) did not perceptably affect the two-dimensionality of the flow over roughly
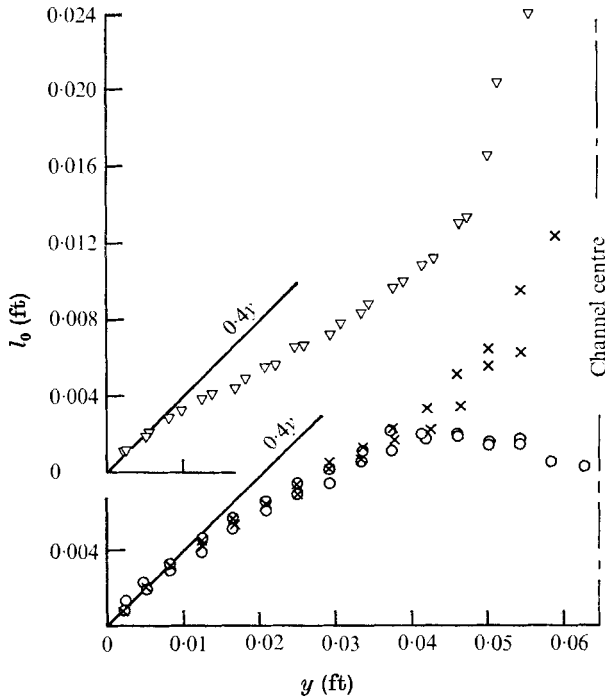
FIGURE 4. Mixing-length profiles at zero rotation. ∇, $Re = 35\,000$, $x/D = 68$; $\bigcirc$, $Re = 11\,500$, $x/D = 68$; $\times$, $Re = 11\,000$, $x/D = 58$.

a four inch span of the side walls on which the experiments were conducted; see the end-view in figure 3.

Although mean velocity profiles indicated the existence of fully developed flow, the mixing-length profiles $l_0(y)$ for zero rotation show that the flow was not quite developed (see figure 4). However, this was not deemed an important restriction on the use of the fully developed two-dimensional flow assumption required to obtain the shear stress profiles from wall stress data.

Flow conditions in the test region of the channel are set when two parameters, Reynolds number and rotation number, are given. Two forms for these parameters were used.

(i) In the visualization tests rotation speed Ω, flow rate Q, and water kinematic viscosity ν (i.e. temperature) were recorded. From the cross-sectional area A of the channel a flow average mean velocity Q/A was formed. Hence, using the characteristic-layer thickness $2D$ (the channel width for developed flow), the practically useful forms of the parameters were obtained:

$$Re_Q \triangleq Q2D/A\nu, \quad Ro_Q \triangleq 2|\Omega|\,DA/Q.$$

(ii) When quantitative results are being discussed it is useful to base these parameters on a velocity scale relevant to the two-dimensional nature of the test-region flow. So U_m, a mean velocity based on the average (from $y = 0$ to $2D$) of the central mean-velocity profile, replaces Q/A, i.e.

$$Re \triangleq U_m 2D/\nu, \quad Ro \triangleq 2|\Omega|\,D/U_m,$$

where
$$U_m = \frac{1}{2D} \int_0^{2D} \bar{u}\,dy.$$

These four parameters were related to each other by use of direct measurements.

The first visualization data were obtained by Halleen (1967). He used the wall-slot dye-injection method developed and shown by Runstadler, Kline & Reynolds (1963) to be valid for study of turbulent wall-layer structure. Halleen made long vertical slots in the transparent test-region side-walls. Very dilute dye-coloured water was caused to seep slowly through these narrow (0·005 in. wide) slots so that dye only penetrated the sublayers. The characteristic wall-layer flow patterns were photographed on a 16 mm. colour motion-picture film (Halleen & Johnston 1966) for a variety of flow conditions. All three stabilization phenomena caused by rotation were observed, but to clarify our information another technique, the hydrogen-bubble method (see Schraub *et al.* 1965), was used by Lezius (1971). Except for figure 11, it is his pictures that we shall present, so a brief discussion of the bubble methods will prove useful.

Lezius first studied wall-layer structure using bubble-generation wires (platinum, diameter 0·001–0·002 in.) set normal to the mean flow and parallel to the wall and the axis of rotation. He was able to show that the tiny bubbles of H_2, when properly generated, followed the flow quite well. Only larger bubbles were subject to sufficient gravitational and 'rotational' buoyancy forces relative to drag forces that they did not mark fluid particle trajectories.

In the main series of tests, one wire was held between traversable prongs so that the wire could be set at arbitrary distances y from one channel wall (see figure 5(a)). By use of mirrors, both the light source and/or camera could be trained on the bubble-marked flow. Two views were adopted: (i) a *plan-view* through the side wall where flow appears to move from left to right in the pictures and the rotation axis (spanwise, or z, direction) is vertical; (ii) an *end-view* where the 'observer' looks upstream into the channel so he sees the flow in cross-section. In all pictures of the latter type the axis of rotation is also vertical.

A special very interesting series of tests were done using two bubble wires (see figure 5(b)). Finally, an over-view of the flow was obtained at low Reynolds numbers using an end-view with a grid of bubble wires set across the whole channel (see figure 5(c)).

Although some of the film data have been examined to obtain the common quantitative measures† of wall-layer structure, these measures have been used primarily to ascertain that our visual observations were proper, and were properly done. The principal quantitative data were taken in addition to the visual observations in order to provide a basis for relating the visual results to the actual quantitative mean-flow behaviour. In brief, mean-velocity profiles $\bar{u}(y)$ were deduced from measured profiles of total (impact, stagnation) and wall static pressure (see figure 6). Wall shear stresses on both side walls were deduced by three different methods. The primary method was the Preston-tube technique. A more detailed discussion of experimental technique is given in the appendix.

Finally, before discussing the results it is useful to consider the ranges and

† Spanwise wall-layer streak spacing λ and streak burst rate (see Kline *et al.* (1967)).
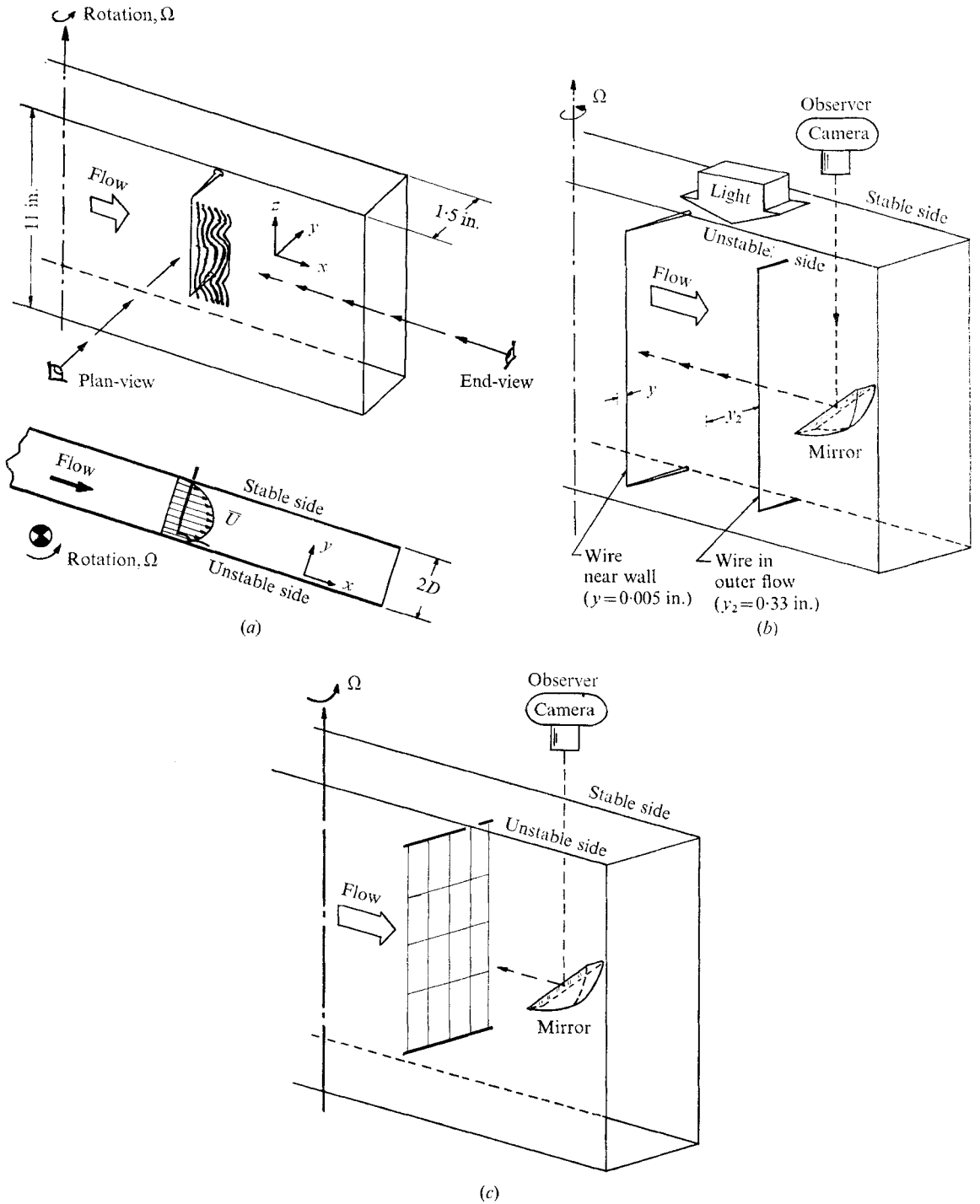
FIGURE 5. (a) Co-ordinates, position of the transverse wire and directions of observation in the rotating channel. (b) Schematic diagram of experimental set up for end-view observation on the unstable side. (c) Wire-grid arrangement for end-view observation of the whole channel cross-section.
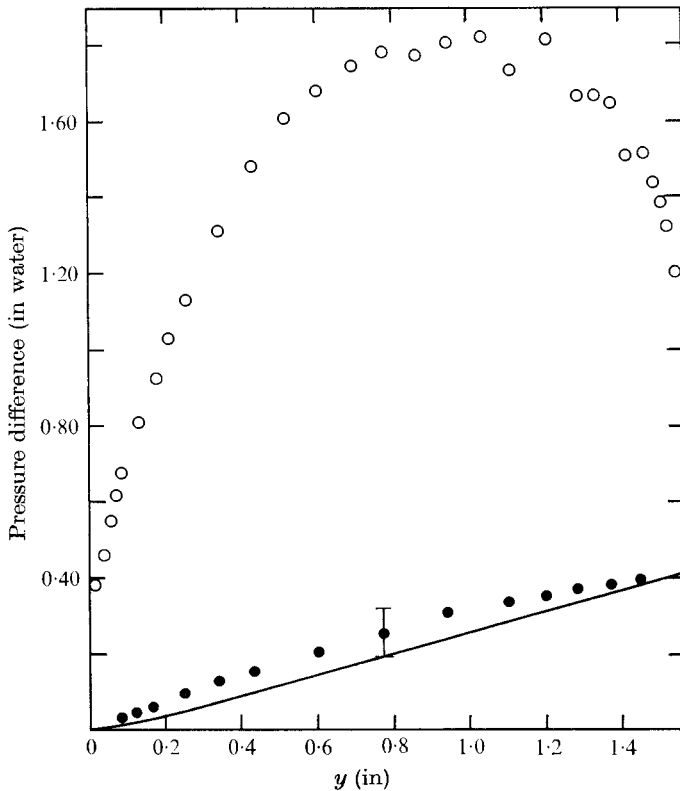
FIGURE 6. Reduced pressure-data profiles at $Ro = 0.08$, $Re = 36000$.
○, total pressure $\Delta \bar{p}^*$; ●, static pressure $(\bar{p}^* - \bar{p}_s^*)$, see appendix.

overlap of ranges of the visual and quantitative data. Because of limits of visual quality imposed by lighting, film speed, etc., no visual data were obtained above $Re = 20000$. Rotative speed limited Ro to values of 0.15 at this Reynolds number, although higher values of Ro were used at low Re. Mean-velocity profiles were all obtained at two Reynolds numbers,

$$Re = 11500 \quad (Ro \leqslant 0.21) \quad \text{and} \quad Re = 35000 \quad (Ro \leqslant 0.081).$$

It is seen that the former set of profile data overlaps with the range of visual results. The wall shear stress measurements were obtained over the same range of Reynolds numbers as that used for the mean-velocity profiles and visual data.

4. Results

This discussion will emphasize the phenomena which we believe are caused by the stabilizing, and destabilizing, influences of the Coriolis forces. As is shown in figure 2, both influences are at work at the same time. Although the stable side of the channel flow is denoted as the region of positive Richardson number and the unstable side as the region of negative Richardson number, precise division into stable and unstable regions is not possible from observed effects. The overall

maximum effects of stabilization are illustrated in figure 7 (plate 1), where the observer looks upstream (end-view) at bubbles generated on a grid of wires that spans the channel (see figure 5(c)). In the two pictures where the channel is in rotation, the stable region is to the right; here the flow appears steady and laminar. The fluid in the unstable region is on the left of each picture, where the flow looks turbulent. As shown in these photographs, and even more clearly in the motion pictures from which they were printed, there is a remarkably sharp line of demarcation or 'interface' between stabilized and destabilized fluid. Vigorous eddies in the turbulent zone appear to collide with this 'interface' almost as though it were a solid wall. Disturbances that do tend to propogate into the stable region are very rapidly damped.†

The results of figure 7 show only the end result of one of the phenomena under investigation, i.e. total laminarization of a stabilized region of a slightly‡ unstable flow. Our plan of discussion is first to present additional visual results that bear on this phenomenon, and how it is affected by both Reynolds number and rotation number. Next, we shall examine some visual evidence concerning the structure of the unstable region where turbulence appears to be enhanced by rotation. Finally, some of the quantitative measurements will be presented and discussed.

4.1. *Rotationally stabilized wall layers*

The structure of the sublayer flow on the stabilized side of the channel is illustrated in the four pictures selected for figure 8 (plate 2). Each is a frame of motion-picture film shot for different conditions of rotation while Re_Q was held approximately constant at 8600. Here, the observer has a plan-view of the wall layers. He sees time lines of bubbles generated on a wire held normal to the mean flow and very close to the wall. The bubble wire is located parallel, and close, to the left-hand edge of each picture.

The zero-rotation picture, $Ro_Q = 0$, clearly shows the wall-layer streak structure described in detail by Kline *et al.* (1967) for turbulent boundary-layer flow. The time-averaged spanwise spacing λ of the streaks of low-speed fluid in figure 8 appears to be roughly $\frac{1}{4}$ in. Halleen (1967) measured λ for a number of different Reynolds numbers and rotation speeds from films made with the dye-visualization method. He found that the streak spacing (non-dimensionalized in wall-layer co-ordinates), $\lambda u_\tau / \nu = \lambda^+ = 98 \pm 15$, being independent of Re_Q and Ro_Q as long as turbulence appeared to be produced in the wall layers. The fact that λ^+ was close to the values obtained in other turbulent flow experiments confirms the 'normalcy' of the conditions of our experiments; Kim, Kline & Reynolds (1971) give $\lambda^+ = 100 \pm 20$ for a number of different turbulent boundary layers.

The turbulent bursting process discussed in detail by Kim *et al.* was evident in the motion-picture films based on either the dye or the bubble method. In

---

† Remember that the damping effect is not primarily due to viscosity but is initiated by the positive 'springiness' of the Coriolis forces.

‡ At zero rotation the transition Reynolds number lies between $Re_Q = 2000$ and 2500 for our channel. Since Re_Q is only 3000 in figure 7 the flow is only marginally turbulent at $Ro = 0$.

figure 8, a burst is evident in the wavy streaks below and to the right of centre in the $Ro_Q = 0.035$ picture (figure 8(b)). It is a widely accepted hypothesis today that these bursts are the source of the largest part of the newly produced Reynolds shear stress and turbulence energy. Processes that tend to reduce the burst rate are expected to reduce stress and energy production. Hence a detailed examination of bursts, their rate of creation and their decay under stabilized and destabilized conditions should yield interesting information on the basic structure of turbulence in bound shear layers. In the preliminary studies reported here only the roughest of observations were possible.

The sequence of pictures in figure 8 illustrates the process of stabilization rather well. In the two pictures at $Ro_Q = 0$ and $Ro_Q = 0.035$, figure 8(a) and (b), the wall layer is fully turbulent. However, even in the fully turbulent region, Halleen (1967) showed, by direct count, that the rate of streak bursting per unit of wall area decreased steadily at Ro_Q increased. This is indirect evidence that the stabilizing effect of rotation is to reduce production of Reynolds stress and turbulence energy if the previously mentioned hypothesis is true. The direct evidence is given in the quantitative data to be discussed later.

The two pictures (figures 8(c) and (d)), at higher rates of rotation, $Ro_Q = 0.082$ and 0.107, represent conditions where the wall layers are only partly turbulent. They will be called 'transitional'. Here laminar† regions are seen, side-by-side with turbulent spots. In the motion-picture films it can be seen that the properties of these spots, in some respects, resemble those of the 'Emmons' type of spots that are typical of the final phase of transition to turbulent flow in a normal boundary layer. Bursting occurs inside the spots. However, the spots do not, on the average, grow and cross-contaminate the flow as they travel downstream in the sublayer. Individual spots may grow to some extent for a limited time, but the effects of growing spots are counterbalanced by the decay of other spots.

The turbulent spots passing a given observation area per unit of time have been counted‡ on the stabilized wall. Lezius's results (figure 9) show the rapid decay of spot passing rate with increases in the degree of stabilization, e.g. increase of Ro_Q. Note also that the phenomenon is Reynolds-number dependent. When no spots were seen for a long period of time both Halleen and Lezius proclaimed that the wall-layer flow was fully laminar; this condition is located at the upper limit line shown on the flow regime chart (figure 10). The lower limit of the transitional region, below which the flow is said to be fully turbulent, is more difficult to define. This lower line is meant to represent a condition where individual laminar regions can no longer be detected in the plan-views of the sublayer. The laminar–streaky limit of Halleen lies slightly above this line. The Halleen limit is now felt to represent a transitional condition and not the limit of fully turbulent wall-layer flow.

The uncertainty in both lines shown in figure 10 is roughly $\pm 15\%$ (20:1 odds) in Ro_Q. The upper limit line was drawn using the Lezius spot-passing-rate data

† Laminar flow is recognized as regions of the wall-layer flow where time lines are parallel to each other.

‡ Counting and observation was carried out directly with the observer riding on the top disk of the rotating apparatus.
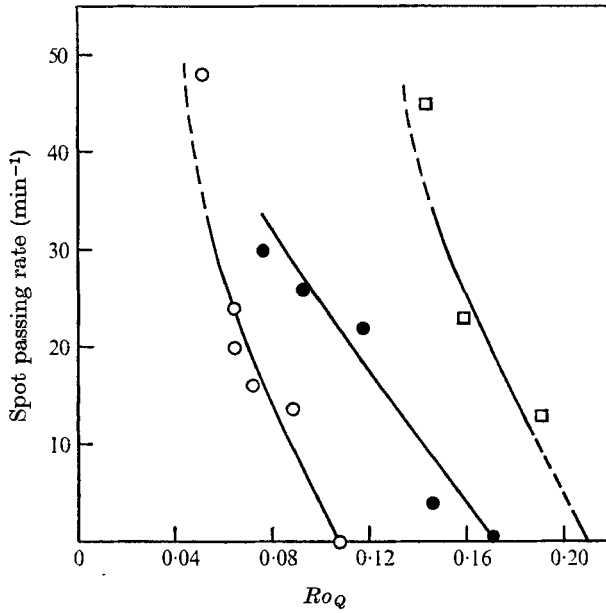
FIGURE 9. Spot passing rate in the transitional zone of the stabilized wall layers. $\bigcirc$, $Re_Q = 5800$; $\bullet$, $Re_Q = 9900$; $\square$, $Re_Q = 15500$.
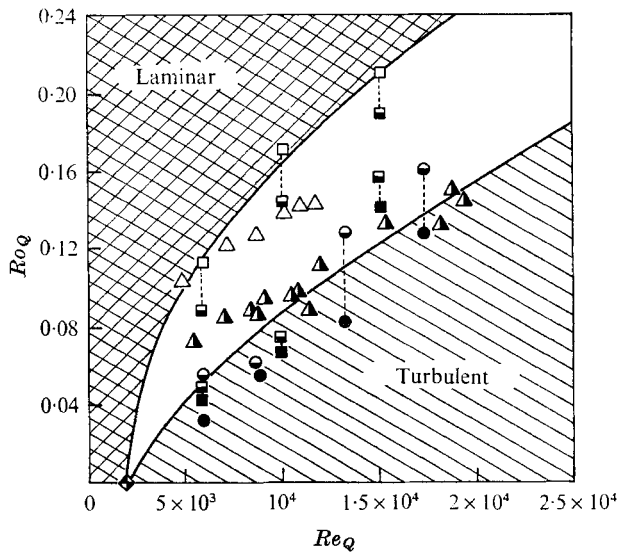

FIGURE 10. Flow regimes in the stable side-wall layers. Direct observations using dye method: $\triangle$, lower limit of laminar flow; $\blacktriangle$, limit of laminar streaky flow. Direct observations using bubble methods: $\square$, laminar flow; $\boxminus$, transitional flow; $\blacksquare$, turbulent flow. Observations from film scenes using bubble methods; $\ominus$, transitional flow; $\bullet$, turbulent flow.

35-2

from figure 9. The lower limit line is traced from a theoretical estimate of the conditions required to maintain fully turbulent conditions (see Johnston 1971). Both lines fit both sets of visual observations to the estimated experimental uncertainty.

Finally, a few notes on the laminar flow regime are of use. The end-view pictures of figure 7 are well above the laminar regime limit of figure 10. They show, as already noted, that turbulence from the unstable side does not essentially penetrate an 'interface'. Dye visualization pictures of the part of the laminar zone right next to the wall showed a steady two-dimensional layer. These observations lead one to the conclusion that nearly all turbulence energy and stress in the channel produced under this condition must come from the unstable wall layer opposite, where bursting is still taking place. In fact, the quantitative data indicate that the turbulent regions adjacent to the 'interface' are regions of negative production of turbulence energy, i.e. $\hat{P} < 0$ next to the 'interface' of figure 7.

4.2. *Rotationally destabilized wall layers*

The basic streak-bursting structure of the wall-layer flow on the destabilized side of the channel was not observed to change with change of rotation number for low rotation numbers, $Ro_Q < 0.02$. However, at $Ro_Q > 0.04$ a new type of structure was clearly observed; a spanwise array of large-scale vortex cells or roll cells which were deduced to be the result of a Taylor–Görtler instability. Photographic evidence for the existence of the roll-cell structure is shown in figures 11–13 (plates 3–5).

Figure 11 (plate 3), from the wall-dye-slot injection studies, shows the general features observed. The four dark, but fuzzy, regions spaced roughly 1.5 in. apart in the spanwise direction were located near the centre-plane of the channel ($y \simeq D$). These dark areas were marked with blue dye that had been injected into the sublayers at an upstream wall slot. The closely spaced streaks, seen downstream of the upstream wall slot and downstream of the second wall slot, where green dye was injected, occur at intervals of length λ, the normal wall-layer streak spacing. In the motion-picture films, bursting of the wall-layer streaks was seen to occur.

The roll-cell structure was first deduced from the dye visualization studies. Fluid in the sublayers is swept along the wall and into an array of regions which are nearly equally spaced in the spanwise (z) direction. The alternate plus and minus spanwise flow can be seen in the angles which the wall-layer streaks make with respect to the four dark regions. Subsequently, the fluid close to the wall is swept away from the wall and deposited in the neighbourhood of the outer edge of the unstable region, i.e. near the channel centre-plane. Fluid returns to the wall regions by sinking toward the wall in the areas between the outflow regions which in figure 11 lie under the four dark fuzzy bands. This flow pattern when viewed end-on looks like a spanwise array of large roll cells. Vortical flow of alternate sign can be seen in each adjacent cell.

Figure 12 (plate 4) shows some further evidence for this hypothesis. Here the pulsed-bubble time-line method was used. Three rotating flows and one stationary flow are shown at roughly the same Reynolds number as the flow shown in

figure 11. However, here all we see are wall-layer effects. In the two high Ro_Q cases there appears to be reduced streakiness and bursting in some areas and increased, or normal, wall-layer activity in others. The areas of reduced activity are also regions of high forward *(u)* velocity as is shown by the large spacing between successive time lines. The calmer regions lie between the areas where the wall layers flow out from the wall. The high velocity in these calm regions results from the convection of high-speed outer-region fluid towards the wall. Finally, the lack of bursting activity in the calm regions may result from the low turbulence levels carried into the wall by the outer fluid. It is suspected that new bursts cannot be triggered if the wall-layer disturbance level is too small.

Figure **13** (plate 5), a set of four end-views obtained using the bubble method, confirms the overall picture outlined above. The larger bubbles came from an upstream bubble-wire set in the sublayer (see figure 5(*b*)). The fine bubbles generated downstream on a second wire in the outer flow were photographed in a manner that clearly illustrates the ejection of wall-layer fluid in the regions where adjacent roll cells cause flow away from the wall. The photographs also show the sinking of outer-layer fluid in the zones where flow in adjacent cells is toward the wall.

Finally, the photographs in figure 13 show the scale of the roll cells relative to channel dimensions. The channel half-width is $\frac{3}{4}$ in., so clearly the cells extend up to, or beyond, the channel centre-plane. Films from which figure 7 was taken indicate that the cells could extend all the way to the turbulent–laminar interface in those cases where total stabilization occurs on the opposite side of the channel. Measurements of the distance between regions where wall-layer fluid enters the outer flow indicated that the combined spanwise size of two cells of opposite rotational sign was roughly 1·2–1·4 in., the order of the total channel width, or two to three times the width of the unstable layer as defined by the Richardson number criteria, see figure **2**.

The conditions for onset of the roll-cell structure were very difficult to define from experiment. Our best estimates from direct observations of bubbles were that recognizable cell structure was present for $Ro_Q > 0·04$ and absent for $Ro, < 0·02$ in the range $6000 < Re_Q < 15000$. Hydrodynamic stability calculation were carried out for turbulent rotating-channel flow by Lezius (1971). He assumed that Taylor–Gortler type disturbances were the proper form of cellular instability, and computed lower critical rotation numbers of $Ro_Q = 0·020$ to 0.025 over the experimental Reynolds number range. Calculations were extended up to $Re, = 35\,000$, where the critical rotation number still fell in the indicated range. Observation of the cells at high Reynolds number was severly limited by the superimposed vigorous small-scale turbulence. Although the calculations carried out by Lezius might be improved by better turbulence models, etc., his results are in good agreement with the observed roll-cell size as well as with the experimental conditions for onset of this large-scale instability.

In the range of Ro_Q where cells are first seen ($0·02 < Ro_Q \leqslant 0·04$), the flow is very unsteady and sometimes cells form, decay, wash-out and wave about in a very unsteady manner. Only at higher rates of rotation are 'steady' cell patterns observed. We call them 'steady' in the sense that the time period over which
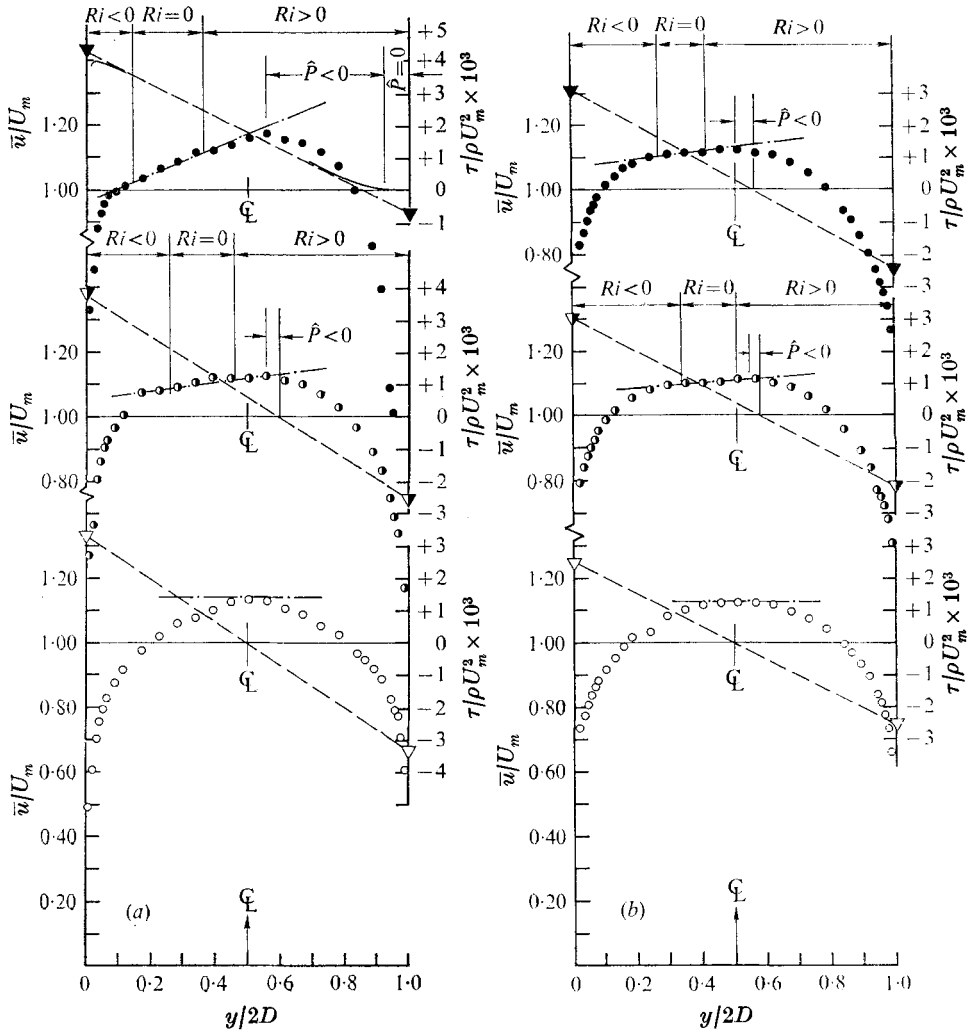
FIGURE 14. Mean velocity and shear stress profiles at $x/D = 68$. ∇, wall shear stress; $\bigcirc$, mean velocity. —·—·, slope of $\xi_{abs} = 0$; ————, total shear stress τ. Open symbols, $Ro = 0$. (a) $Re = 11\,500$. Half-filled symbols, $Ro = 0.069$; filled symbols, $Ro = 0.210$; solid curves for $Ro = 0.21$ are estimate of $-\rho\overline{u'v'}$ where it differs significantly from τ. (b) $Re = 35\,000$. Half-filled symbols, $Ro = 0.42$, filled symbols, $Ro = 0.068$.

a given pattern persists is long relative to the turbulence time scales.† However, in no case did we ever observe a truly steady cell pattern. It was thought that the unsteadiness was caused by the turbulent fluctuations, or by end effects due to the finite aspect ratio of the channel.

4.3. Quantitative results

Selected mean velocity profiles are presented in figure 14 (a) and (b). Superimposed on these figures are dashed lines representing the total shear stress profiles deduced from the wall shear stress data.

† However, at low Reynolds numbers, $Re \simeq 3000$ say, both time and length scales of wall-layer streaks and vortex cells are about the same.

The two velocity profiles at zero rotation are symmetrical about the channel centre-plane, whereas the shear stress is antisymmetric. Mixing-length profiles deduced from these data are shown in figure 4. In the central third of the channel there is some indication that the flow at $Re = 35\,000$ and $x/D = 68$ may not be quite fully developed. Hence conclusions based on our data from this central region must be viewed as qualitative. However, in the wall layers the shear stress model is much more reliable and results are of quantitative value.

In the rotating cases shown in figures 14(a) and (b) we have divided the flow into unstable, neutral and stabilized regions according to the local stability criteria based on the Richardson number. The mean profiles tend to show sizeable regions of neutral stability, where $Ri = 0$, or alternatively, regions where the mean vorticity relative to inertial co-ordinates is zero, i.e.

$$\xi_{abs} = 2\Omega - d\bar{u}/dy = 0. \tag{9}$$

Since the flow entering the channel is fully rotational† there is no clear reason why a region, rather than a single point of $\xi_{abs} = 0$, should appear to divide the stable from the unstable side of the flow. The width of the neutral region is hard to determine accurately. However, the figures tend to show that it is slightly larger at the lower Reynolds number than at the higher. The significance of this observation, if true, is still to be deduced.

Perhaps more relevant is the observation that as Ro increases the size of the stable region increases. In all cases shown in figures 14(a) and (b) except one, that at $Re = 11\,500$ and $Ro = 0.210$, both wall layers are in the turbulent flow regime. In the special case a significant laminar region exists on the stable side.

Ro is high enough, for the data shown, for there to be roll cells on the unstable side of the channel. Even though the size of the region of local instability decreases as Ro increases, this decrease does not appear to affect the size of the large-scale roll cells which extend into the region of local stability for the flows shown. These observations emphasize the fundamental difference between small-scale, local instability and the instability on a large scale which leads to the roll cells. Large-scale instability leads to 'global' effects. In the wall layers, however, events are largely under the control of local conditions. Here we can expect the local stability parameter Ri, or the parameter S, to be the dominant independent parameter that controls structure-related quantities such as the mixing length.

Regions of negative turbulence production $\hat{P}$ are seen in all the rotating-flow cases of figures 14(a) and (b). In all but one case, these regions are narrow and located in the central areas of the channel where $\hat{P}$ is very small compared with its magnitude in the regions of intense turbulence production near the walls.

As already noted, at $Re = 11\,500$ and $Ro = 0.210$ the stable side-wall layer is laminar. For this case, solid curves are drawn in figure 14(a) to mark an estimate of the turbulent stress profile. In the laminar region, near the stable wall, this stress profile shows a significant laminar region, where $\hat{P} = 0$. Next to the laminar region is a very thick area in which turbulence energy, convected and diffused from the unstable side of the channel, is not only dissipated but also converted back into mean kinetic energy by negative production.

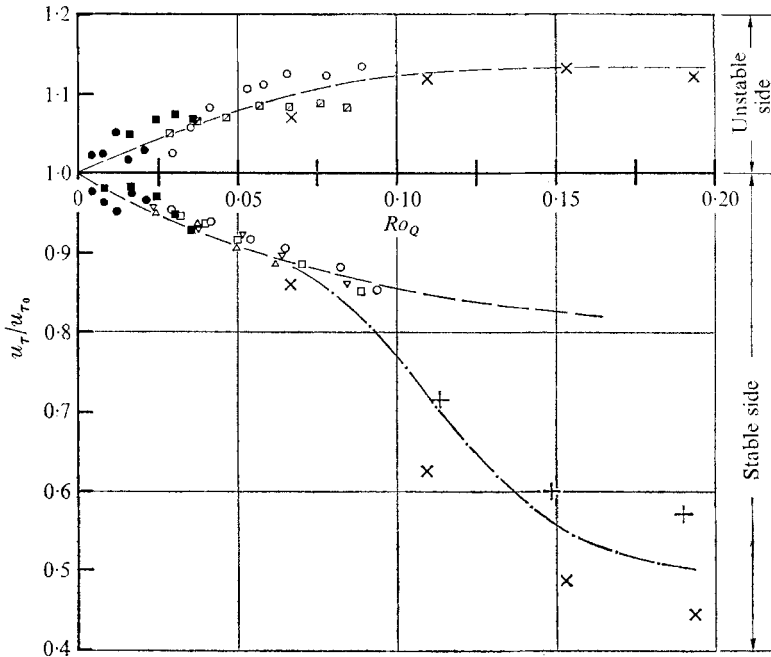† $d\bar{u}/dy = 0$ and $\xi_{abs} = 2\Omega$ at the upstream honeycombs.

FIGURE 15. Wall-shear velocity normalized on zero-rotation values at equal Reynolds numbers. Data based on Preston-tube method: □, $Re_Q = 23400$; ○, $Re_Q = 25700$; ◩, $Re_Q = 33100$; △, $Re_Q = 34800$; ▽, $Re_Q = 36000$. Data based on wall slope and law of the wall methods: +, $Re_Q = 10300$; ×, $Re_Q = 11400$. Filled symbols are from 7·33 aspect ratio channel of Moore (1967). — — —, behaviour expected when both wall layers turbulent; — · — · —, behaviour of stable side transitional wall layer at $Re \simeq 10^4$.

The wall shear stress data are displayed in figure 15. Data for a range of Reynolds numbers are shown. Included are some air-flow Preston-tube data taken by Moore (1967) on a rotating channel nearly identical in geometry to our channel.

At zero rotation the wall shear stress coefficient measured in the central two-dimensional flow region fits the equation

$$c_{f0} = 2\tau_{w0}/\rho U_m^2 = 0\cdot 0706 Re^{-0\cdot 25} \tag{10}$$

to better than ± 7 % over the full range of the data. This result, to the indicated uncertainty, is in agreement with other recent channel data at high aspect ratio, the only significant exception being the results of Patel & Head (1969) at $Re > 4000$.

No strong clearly identifiable Reynolds number effect can be seen in the data of figure 15 for low rates of rotation, $Ro_Q \leqslant 0\cdot 08$–$0\cdot 10$. The rapid drop of u_τ for the low Reynolds number points on the stable side is certainly due to the fact that transition from turbulent to laminar flow occurs over the range $0\cdot 08 < Ro_Q < 0\cdot 16$ at $Re_Q = 10000$ (see figure 10). At the higher Reynolds numbers wall shear stress on the stable side would probably extrapolate along the dashed curve until Ro_Q became large enough to cause transition back to laminar flow.

We suspect, but cannot prove, that the apparent levelling off of the wall shear velocity on the unstable side of the channel between $Ro_Q = 0\cdot 05$ and $0\cdot 15$ may
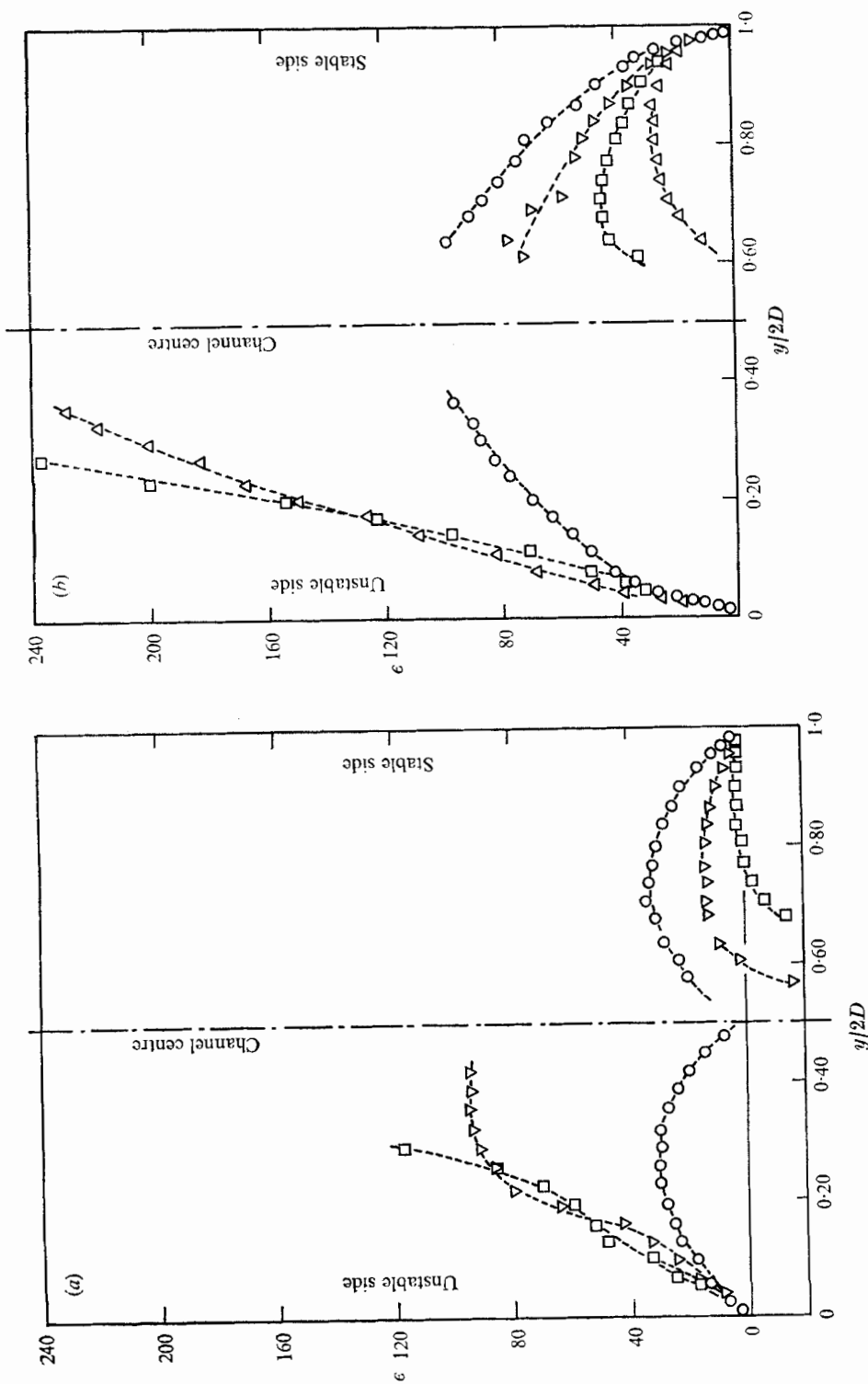
FIGURE 16. Turbulent eddy viscosity. (a) $Re = 11500$; $\bigcirc$, $Ro = 0$; $\triangledown$, $Ro = 0.069$; $\square$, $Ro = 0.117$. (b) Turbulent eddy viscosity at $Re = 35000$; $\bigcirc$, $Ro = 0$; $\triangledown$, $Ro = 0.027$; $\square$, $Ro = 0.042$; $\triangle$, $Ro = 0.081$.

result from the final phase of development of the roll cells. Once these cells become a dominant feature of the flow they may inhibit the streak-bursting process and thus limit the increase of u_τ on the unstable wall. It is hypothesized that the strong transverse, or spanwise, flows in the wall layers under the cells sweep a fraction of the bursting streaks into the outflow regions before they can break down and produce extra turbulence energy and stress. As has already been pointed out in § 4.2, the inflow of lower turbulence outer fluid provides another reason to believe that bursting may be inhibited in regions between the roll-cell outflows. Whatever reason prevails, it seems clear that the full development of roll cells limits the increase of turbulent stress and energy produced by the increase of local instability as Ri grows.

The effects of local stabilization and destabilization on mixing length have been shown and discussed previously (see Johnston 1971). To a good approximation, the 'Monin–Oboukhov' type of relationship suggested by Bradshaw (1969),

$$l/l_0 = 1/(1 + \beta Ri) \simeq 1 - \beta Ri, \tag{11}$$

fits our data in the range $0 < |Ri| < 0.25$ for values of $\beta = 6 \pm 2$. l_0 in (11) is the mixing length at zero rotation (see figure 4). This result is limited to cases where the wall layers are fully turbulent. Because of the uncertainties in the data, it cannot be ascertained if the ratio l/l_0 is not also slightly dependent upon Ro and Re as well as upon the local stability parameter Ri.

The profiles of eddy viscosity ϵ deduced from some of the data are shown in figures 16(a) and (b). The data in the central regions of the channel

$$(0.3 < y/2D < 0.7)$$

is of high uncertainty because of (i) the difficulty of accurate measurement of $\partial \overline{u}/\partial y$ and (ii) the possible failure of the flow to be fully developed for the $Re = 35\,000$ cases.

In the low Re flow (figure 16(a)), negative values of eddy viscosity are coincident with regions of negative turbulence production $\hat{P}$ (see (7)). In the flow at $Ro = 0.117$, $\epsilon = 0$ near the stable wall. This is clear evidence of the total laminarization of the stabilized wall layers for this case.

In both figures 16(a) and (b) the values of ϵ near the unstable walls are larger than at zero rotation, but appear to be only weakly dependent on Ro. In all cases shown, Ro is high enough to give well-developed roll cells. The lack of dependence of ϵ on Ro near the unstabilized side is further evidence for the point made already, namely that roll cells provide a mechanism for limiting the growth of turbulent stress in locally unstable regions.

5. Summary of conclusions

Certain conclusions of a general nature can be drawn from the results. First, three different stabilization phenomena were observed by visual means in the channel flow. It is believed that these phenomena will also be observed in rotating boundary layers. Second, the nature of these phenomena is clarified by the quantitative data which, to a limited extent, also provide some empirical information for boundary-layer prediction methods.

The three rotation-induced phenomena are: (i) the reduction (increase) of turbulent wall-layer streak bursting rate in locally stabilized (destabilized) layers; (ii) the total suppression of turbulence production in the locally stabilized layer; and (iii) development of the roll cells on the destabilized side of the channel.

As expected, the gradient Richardson number Ri appears to be the appropriate parameter to characterize the state of local stability in a turbulent shear layer. $Ri > 0$ indicates stability and $Ri < 0$ indicates instability in a given layer of a shear flow. The rotation number Ro could be interpreted as an average, or mean, stability parameter for a whole layer, but here it is viewed as a scalar number whose size controls the magnitude of the ratio of Coriolis to inertial forces. Ro is also used to parameterize the onset of phenomenon (ii) above (see figure 10), and the condition where the roll cells, phenomenon (iii), start to form in the turbulent channel flow, i.e. at a critical value $Ro = 0.02$–0.04.

Phenomenon (i), reduction of wall-layer streak bursting in locally stabilized layers, has been shown to be associated with reduction of Reynolds stress, eddy viscosity and turbulence energy production in the wall layers. Although increases in Reynolds stress, etc., were noted in destabilized layers no direct visual evidence of increased bursting activity in destabilized layers could be obtained. Nevertheless, it is presumed that increased burst rates must be occurring in the destabilized layers at least for low magnitudes of Ro.

The full development of roll cells at $Ro > 0.05$–0.10 may limit the increase of bursting in the destabilized wall layers. This effect appears to be confirmed in some of the visual evidence, and offers a basis for explanation of the limited rate of increase of stress and eddy viscosity at higher rates of channel rotation.

Phenomenon (ii), laminarization of the locally stabilized layer, is discussed at length in Johnston (1971), where a simple theoretical method for extrapolation of the lower limit line in figure 10 is offered.

When laminarization occurs on the stable side of the channel, an extensive region of negative rate of turbulence energy production was observed adjacent to the laminar wall layer. In this region, mean-flow energy is produced at the expense of turbulence energy, an interesting phenomenon not often encountered. Rotating-channel flow may offer a good vehicle for investigation of negative rate of turbulence energy production.

Finally, phenomenon (iii), the development of the roll cells on the destabilized side of the channel, is not unexpected on theoretical grounds. They are another realization of Taylor–Gortler instability. Roll cells have been encountered in turbulent layers that flow over concave walls. An interesting example of roll-cell development is seen in the experimental work of Kaye & Elgar (1957) on turbulent axial flow in the annular gap between an outer stationary cylinder and an inner cylinder that rotates about its axis of revolution. In our discussion, we have concentrated on the qualitative characteristics of the roll cells. Further discussion is deferred to a future paper.

Appendix

The mean-velocity profiles could have been deduced directly from dynamic pressure $\frac{1}{2}\rho\bar{u}^2$, obtained from local total $(\overline{p_0^*})$ and local static $(\overline{p^*})$ pressure profiles. Static pressure varies nonlinearly across the channel when it is rotating (see $(2b)$). However, measurement of $\overline{p^*}$ profiles was rather difficult, and subject to high uncertainties. Hence an iterative procedure was devised for determination of $\frac{1}{2}\rho\bar{u}^2$. This procedure required only the measured value of $\Delta p^* = \overline{p_0^*}(y) - \overline{p_s^*}$, the difference between total pressure and wall static pressure on the stable† (low-pressure) wall, the rotative speed Ω and channel mean velocity Q/A. For a first approximation $\bar{u}$ was assumed constant and equal to Q/A so that integration of $(2b)$ gave

$$\overline{p^{*(1)}} - \overline{p_s^*} = -2\Omega(Q/A)(y - 2D), \tag{A 1}$$

a first approximation to the local static pressure. $\overline{p^{*(1)}}$ was then used to obtain a first approximation to local dynamic pressure:

$$\tfrac{1}{2}\rho\bar{u}^{(1)2} = \Delta p^* - [\overline{p^{*(1)}} - \overline{p_s^*}]. \tag{A 2}$$

The $\bar{u}^{(1)}$ profile was subsequently integrated to obtain $U_m^{(1)}$, which, when substituted for Q/A in (A 1), gave a new approximation for $\overline{p^*}$ and hence for $\bar{u}$ when combined with measured Δp^* in (A 2). This process was repeated until successive changes in calculated $\bar{u}(y)$ profiles were less than 1 %. At that point, the nonlinear static pressure profile $\overline{p^*}$ was determined by numerical integration of $(2b)$ where $\overline{v'^2}$ was again neglected. The values of $\overline{p^*}$ so obtained were fed back into (A 2) and iteration continued until successive $\bar{u}(y)$ profile changes were again less than 1 %. Finally, a gradient displacement effect (McMillian 1957) for the total pressure probe (0·0355 in. in diameter) was added to the mean velocity profile points near the channel walls.

A typical raw $\Delta p^*(y)$ profile is shown in figure 6. The solid line is the final iterated calculation of the static pressure profile $\overline{p^*}(y)$. It is compared with an actual static-tube measurement of the $\overline{p^*}(y)$ profile. The uncertainties in the measured $\overline{p^*}$ values were estimated to be larger than the uncertainties in the calculated profile.

The principal method for measurement of wall shear stress was the Preston-tube technique. It had been used previously in rotating-boundary-layer air-flow studies by Hill & Moon (1962) and by Moore (1967). They found, as did Halleen for our conditions and tube sizes (diameter d), that results were not effectively different from those obtained by the standard zero-rotation correlations even when the additional dimensionless parameter $\Omega d^2/\nu$ was independently varied. Hence, the direct calibrations for our tubes at zero rotation based on the measured

† Stable and unstable walls are referred to as trailing and leading walls respectively by Halleen and Lezius. In this analysis Ω is positive and $y = 0$ on the unstable wall.

axial pressure gradient dp/dx could have been used to compute wall stress under rotating conditions. In fact, these calibrations were in excellent agreement with the Patel (1965) correlation which was used in final data reduction.

Wall shear stresses were, in a few cases, also deduced from the mean-velocity profiles by means of the zero-rotation 'law of the wall'†

$$\bar{u}/\bar{u}_\tau = 5\cdot8 \log_{10} (y\bar{u}_\tau/\nu) + 5\cdot0,$$

when the flow was turbulent.

When thick laminar sublayers or laminar flow existed, direct measurement of the profile slope, extrapolated to the wall, provided an estimate of the wall shear velocity:

$$\tau_w/\rho = \bar{u}_\tau^2 = \nu(\partial\bar{u}/\partial y)_{y=0}.$$

The uncertainty levels on the wall shear stresses obtained by either of the latter methods was fairly high, but the trends of the results appear valid when considered in conjunction with the visual data.

REFERENCES

BRADSHAW, P. 1969 *J. Fluid Mech.* **36**, 177–191.

BRADSHAW, P., FERRISS, D. & ATWELL, N. 1967 *J. Fluid Mech.* **28**, 593–616.

DEAN, R. C. 1968 Advanced centrifugal compressors. *A.S.M.E. Special Publ.* no. H. 38.

HALLEEN, R. M. 1967 Ph.D. dissertation, Mech. Engng Dept., Stanford University.

HALLEEN, R. M. & JOHNSTON, J. P. 1966 Film: Flow in a long rotating rectangular channel. *Engng Soc. Library, ASME–ESL Catalogue Motion Pictures Res. Data in Fluid Mech*, item J-I.

HART, J. E. 1971 *J. Fluid Mech.* **45**, 341–352.

HILL, P. G. & MOON, I. M. 1962 *Gas Turbine Lab., M.I.T.* no. 69.

JOHNSTON, J. P. 1970 *Thermosciences Div., Mech. Engng Dept., Stanford University Rep. MD-24.* (To be published in *N.A.S.A. Special Paper*, no. 304.)

JOHNSTON, J. P. 1971 *AGARD Conference on Turbulent Shear Flows, AGARD Current Paper*, no. 93.

KAYE, J. & ELGAR, E. C. 1957 *Trans. A.S.M.E.* **58**, 753–765.

KIM, H. T., KLINE, S. J. & REYNOLDS, W. C. 1971 *J. Fluid Mech.* **50**, 133–160.

KLINE, S. J., REYNOLDS, W. C., SCHRAUB, F. A. & RUNSTADLER, P. W. 1967 *J. Fluid Mech.* **30**, 741–773.

LEZIUS, D. K. 1971 Ph.D. dissertation, Stanford University. (See also *Thermosciences Div., Mech. Engng Dept., Stanford University Rep. MD-29.*)

MCMILLIAN, F. A. 1957 *Aero Res. Counc. R. & M.* no. 3028.

MOORE, J. 1967 *Gas Turbine Lab, M.I.T. Rep.* no. 89.

PATEL, V. C. 1965 *J. Fluid Mech.* **23**, 185–208.

PATEL, V. C. & HEAD, M. R. 1969 *J. Fluid Mech.* **38**, 181–201.

POTTER, M. C. & CHAWLA, M. D. 1971 *Phys. Fluids*, **14**, 2278–2281.

RUNSTADLER, P. W., KLINE, S. J. & REYNOLDS, W. C. 1963 *Thermosciences Div., Mech. Engng Dept., Stanford University Rep. MD-8.*

SCHRAUB, F. A., KLINE, S. J., HENRY, J., RUNSTADLER, P. W. & LITTELL, A. 1965 *Trans. A.S.M.E.* D **87**, 429–444.

TOWNSEND, A. A. 1956 *The Structure of Turbulent Shear Flow.* Cambridge University Press.

† Consideration of the law of the wall in rotating flow is given in Bradshaw (1969), and in more detail in the discussion and closure of Johnston (1970). For cases considered here rotation effects are small below $yu_\tau/\nu = 100$.
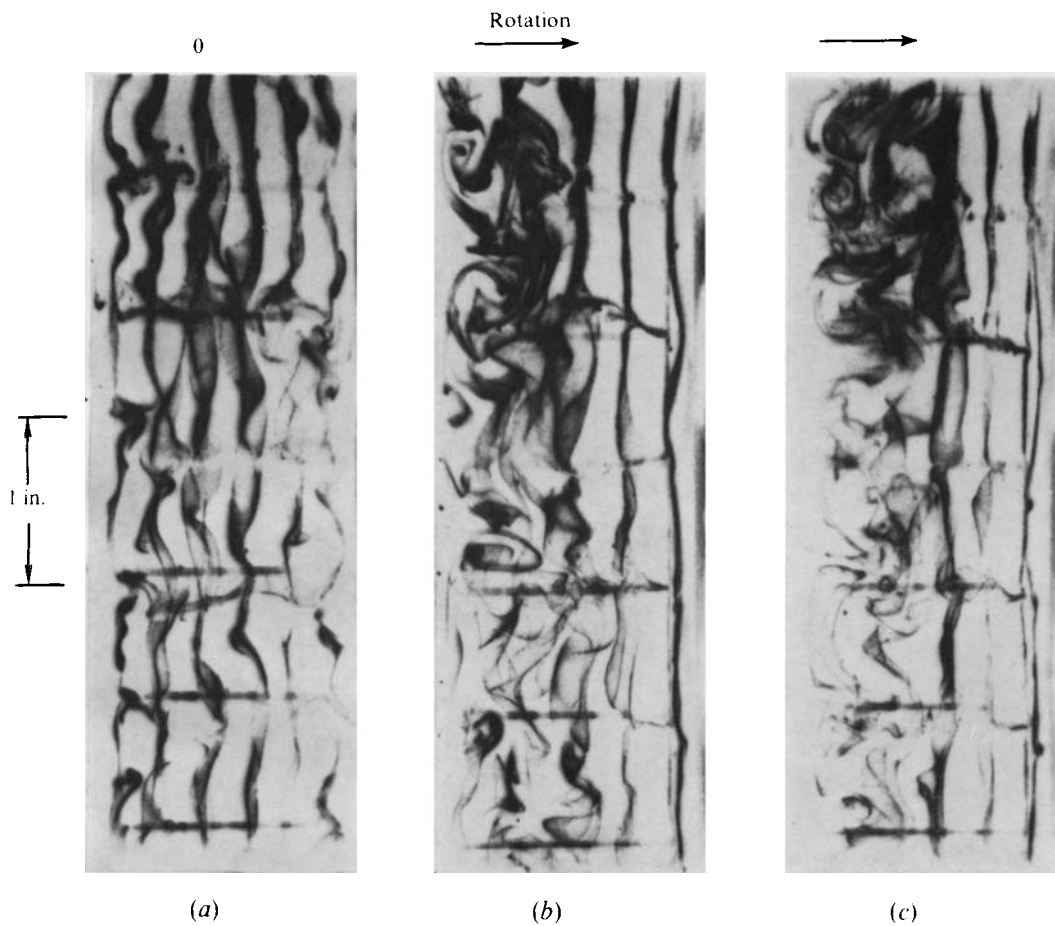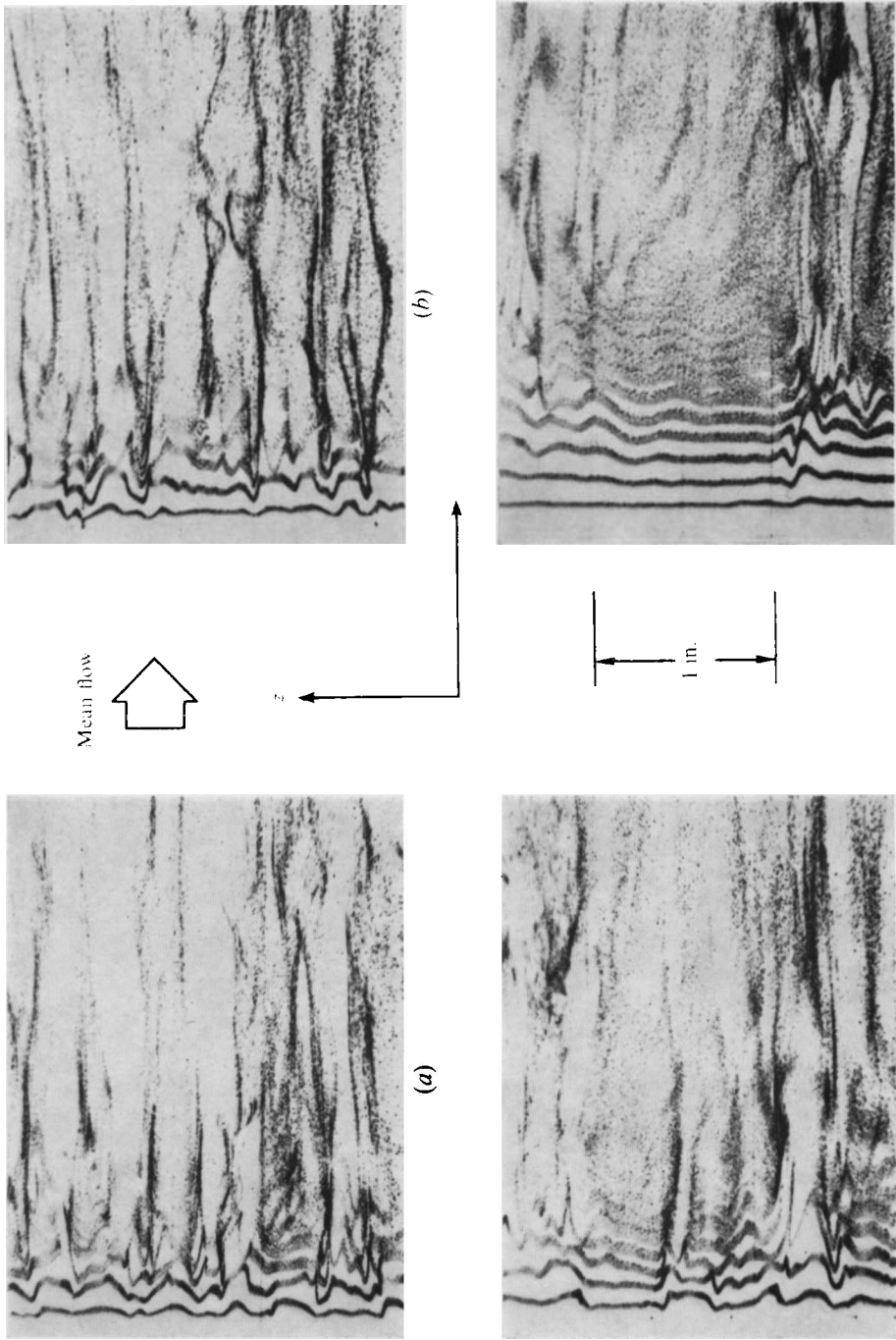
FIGURE 7. Hydrogen-bubble traces downstream of grid (see figure 5(c)). Rotation axis vertical. Unstable side to the left, stable side to the right. $Re_Q = 3000$. (a) $Ro_Q = 0$. (b) $Ro_Q = 0.27$. (c) $Ro_Q = 0.57$.

Plate 2

Mean flow

z

1 m.

FIGURE 8. Hydrogen-bubble time lines in stable wall layer. $Re_Q = 8600$. Wire position at $y = 0.005$ in., $y^+ = 1.6$. Plan-views, see figure 5(a). (a) $Ro_Q = 0$. (b) $Ro_Q = 0.035$. (c) $Ro_Q = 0.082$. (d) $Ro_Q = 0.107$.
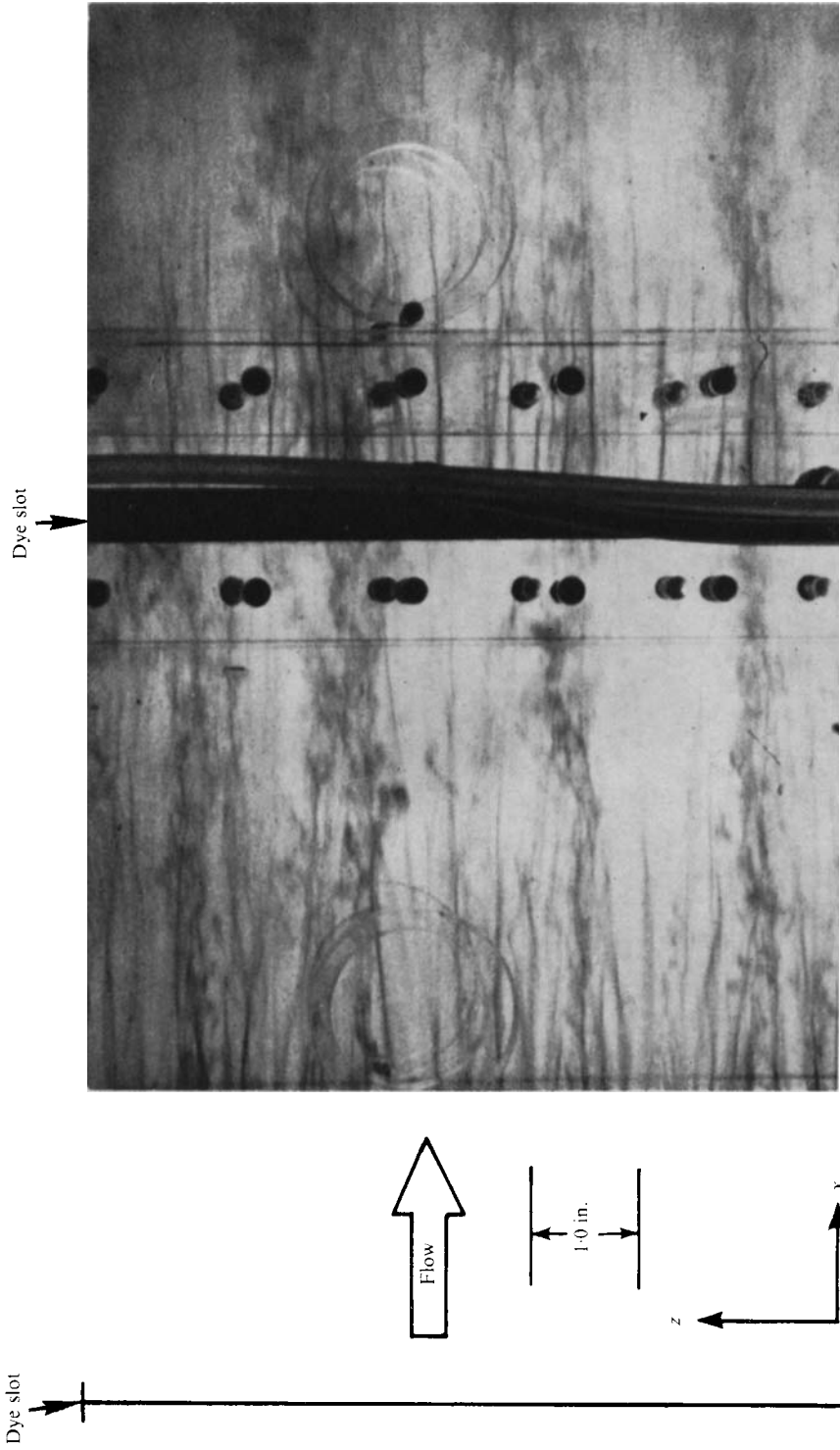
FIGURE 11. Dye patterns on the destabilized side of the channel at $Re = 8800$ and $Ro = 0.176$.
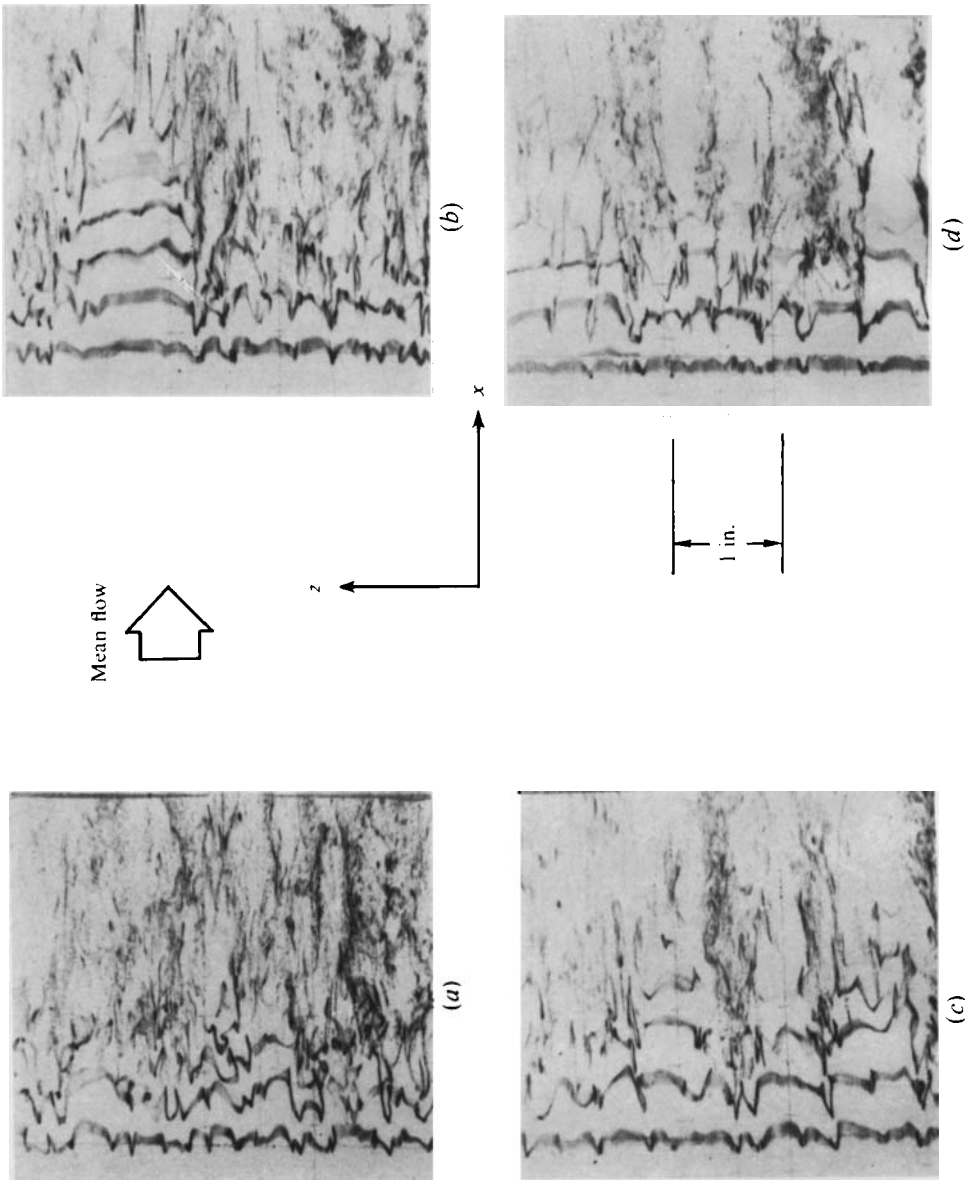
Dye slot

Flow

1·0 in.

x

z

Dye slot

FIGURE 12. Hydrogen-bubble time lines in unstable wall layer. $Re_Q = 9800$. Wire positions at $y = 0.020$ in., $y^+ = 8$. (a) $Ro_Q = 0$. (b) $Ro_Q = 0.084$. (c) $Ro_Q = 0.142$. (d) $Ro_Q = 0.197$.
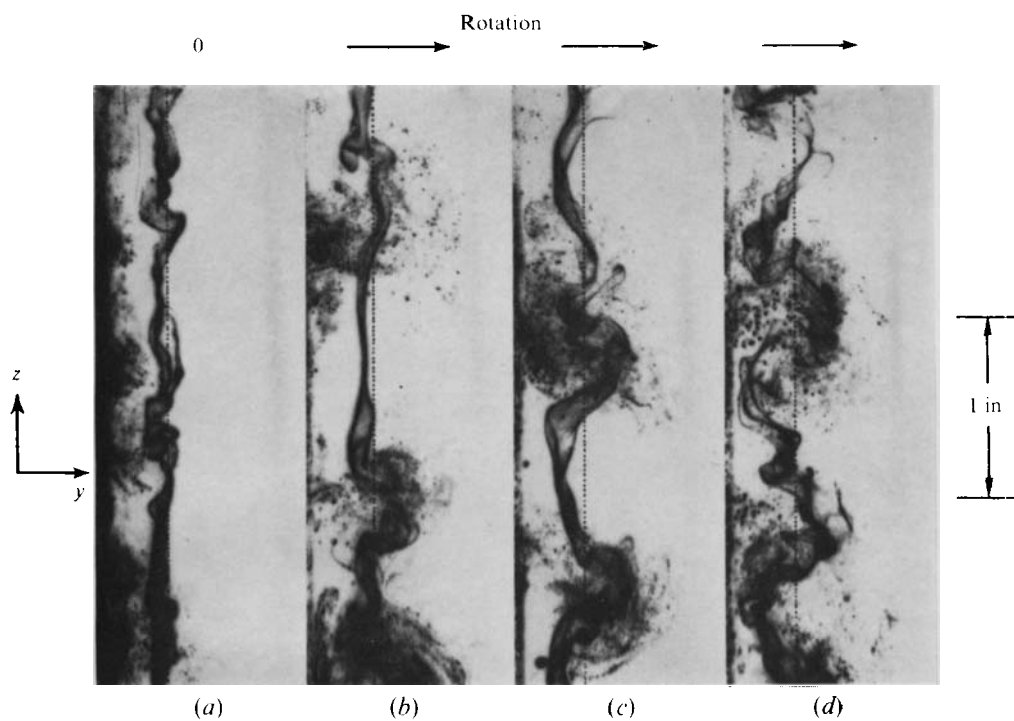
FIGURE 13. End-view of roll-cell structure on unstable side at $Re_Q = 5900$. Bubble wires and view as shown in figure 5(*b*). Photos taken 0·23 s after release of bubbles from downstream wire at position shown by dotted line. (*a*) $Ro_Q = 0$. (*b*) $Ro_Q = 0·22$. (*c*) $Ro_Q = 0·32$. (*d*) $Ro_Q = 0·49$.